ASME Letters in Dynamic Systems and Control
Online journal at:
https://asmedigitalcollection.asme.org/lettersdynsys

Rapid Airborne Gas-Plume Mapping and Source Localization With Feedforward Gas-Sensor Dynamics Compensation

Kyle C. Hoffman
Dynamic Autonomous Robotics (DARC) Lab,
Department of Mechanical Engineering and
Robotics Center,
University of Utah,
Salt Lake City, UT 84112
e-mail: Kyle.C.Hoffman@utah.edu

Jacob M. Anderson
Dynamic Autonomous Robotics (DARC) Lab,
Department of Mechanical Engineering and
Robotics Center,
University of Utah,
Salt Lake City, UT 84112
e-mail: jacob.m.anderson@utah.edu

Kam K. Leang[1]
Fellow ASME
Dynamic Autonomous Robotics (DARC) Lab,
Department of Mechanical Engineering and
Robotics Center,
University of Utah,
Salt Lake City, UT 84112
e-mail: kam.k.leang@utah.edu

This article focuses on improving the speed, accuracy, and robustness of autonomous aerial-based chemical sensing for plume mapping and source localization through characterizing, modeling, and feedforward compensation of gas-sensor dynamics. First, the dynamics of three types of gas sensors are modeled. Second, the maximum chemical-mapping speed is calculated and shown to be inversely proportional to sensor time constant. Third, an inversion-based approach is used to compensate for the sensor dynamics to improve mapping throughput. Results show that dynamics compensation enhances the chemical-mapping speed by over five times compared to the uncompensated case. Finally, to further demonstrate utility, the approach is applied to a particle swarm optimization example for plume-source localization. The improvement is observed by how well the agents converge to the true chemical gas source location when gas-sensor dynamics are taken into account. Specifically, for a static Gaussian plume source, feedforward compensation leads to 64% average improvement in localization success, and for a dynamic Quick Urban and Industrial Complex (QUIC) dispersion plume source, a 39% average improvement is observed. These results underscore the importance of sensor dynamics compensation for enhancing mapping and source localization throughput, accuracy, and robustness.
[DOI: 10.1115/1.4066513]

Keywords: chemical sensing, source localization, plume tracking, feedforward control, autonomous systems, robotics, uncrewed vehicles

1 Introduction

Fast and effective chemical plume mapping and source localization are crucial for minimizing the impact, cost, and recovery time of accidental events or malicious attacks that involve chemical, biological, nuclear, radiological, and/or explosive (CBNRE) substances [1]. Recent advancements in low-cost mobile robotic systems, such as uncrewed aerial vehicles (UAVs) in the form of small fixed-wing and hover-capable rotorcraft vehicles, have attracted the attention of the academic, government, and industry communities to exploit these systems for autonomous CBNRE detection, monitoring, and localization [2–4]. One of the major challenges in robotics-based olfaction and gas-leak localization is the limited performance of the chemical-sensing system, where the majority of available sensors for detecting the presence of chemical substances have relatively slow response time in the seconds to tens-of-seconds range. To advance the state-of-the-art, the contribution of this paper is the characterization, modeling, and feedforward compensation of gas-sensor dynamics to enable rapid and effective chemical mapping and source localization. The majority of hover-capable UAVs that are being exploited for such tasks are limited in power and flight time. Thus, by understanding the impact of sensor dynamics and leveraging sensor models and feedforward compensation, it is shown that the mapping and localization speed can be greatly enhanced for broad real-world applications.

Figure 1 shows a typical scenario for the deployment of an autonomous aerial-robotic CBNRE detection and localization system to find dangerous leaking chemical gas sources. In recent years, similar systems have been deployed to detect, find, and map CBNRE leaks and spills [1,5]. These systems are designed with autonomous navigation, automatic collision avoidance technology, inter-unit communication, and integrated ground station control and data processing [5]. Algorithms have been developed for gas source localization (GSL) and gas distribution mapping (GDM) for applications that include environmental monitoring [1,6], pollution monitoring [7], and search and rescue operations [8]. Compared to ground-based mobile robots, aerial-based systems can more easily navigate over rough and complex terrain; and they can quickly move in three-dimensional space. However, one major disadvantage of multi-rotor, hover-capable aerial platforms is the limited flight and operation time [9]. Therefore, efficient and effective GSL and GDM algorithms coupled with high-performance, high-bandwidth on-board CBNRE sensors are desirable. Unfortunately, the majority of readily-available low-cost CBNRE sensors have low bandwidth which can make the GSL and GDM process slow. For example, slow response and delays

[1]Corresponding author.
Manuscript received July 12, 2024; final manuscript received September 4, 2024; published online September 27, 2024. Assoc. Editor: Yen-Chen Liu.

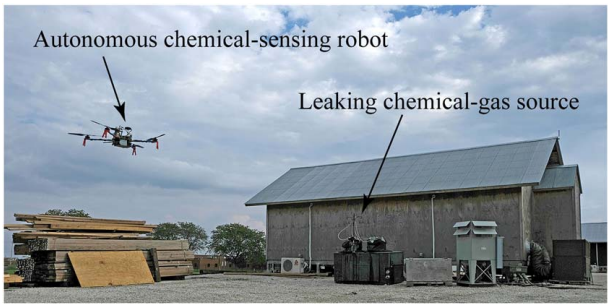

Fig. 1 Autonomous chemical-sensing aerial robot deployed to sense, detect, and localize a leaking chemical source

in reporting the true temporal and spatial chemical concentration, especially when coupled with the relatively fast dynamics of an aerial platform, can result in mapping, localization, and plume tracking inaccuracies, as well as distortions in the resulting chemical concentration map. Herein, the dynamics of three example sensors are characterized and modeled, and a feedforward frequency-domain approach is exploited to improved GDM and GSL.

State-of-the-art approaches to deal with sensor dynamics issues include: (1) limiting the velocity of the robotic platform, on the order of 0.02–0.05 m/s [10], (2) implementing wait times at each measurement point when creating a map, typically between 5 and 20 s [10], and (3) designing trajectories for data collection which roughly cover the desired area while also ensuring redundant measurements. The latter approach effectively updates cells multiple times and thus indirectly compensates for slow sensor response, resulting in improved spatial mapping accuracy. Herein, a frequency-domain model inversion process is used to compensate for the sensor dynamics to improve the performance of GSL and GDM. The main contributions of this work include: (1) characterizing and modeling three different types of gas sensors, (2) developing and implementing feedforward compensation to account for sensor dynamic-induced errors for mapping as well as source localization, and (3) studying the impact of sensor dynamics on particle swarm optimization for multi-agent mapping and source localization.

2 Technical Approach

2.1 Chemical Gas-Sensor Model. The three gas-sensor technologies under consideration are shown in Fig. 2: (1) metal oxide (MOX) gas sensor (Hanwei Electronics/Grove MQ2), (2) nondispersive infrared (NDIR) gas sensor (Euro-Gas Management Services P4 series), and (3) the newly developed molecular property spectrometer (MPS) chemical sensor (Nevada NanoTech Systems, Inc.). These sensors were chosen because they are commonly used in environmental monitoring applications and the detailed characterization can be further exploited to improve GSL and GDM algorithm development. Additionally, the results presented here can be directly applied to other gas sensors available on the market with similar behavior.

The MOX gas sensor is suitable for the detection of propane and a number of other flammable gases including liquefied petroleum gas, isobutane, methane, alcohol, and hydrogen. The sensor utilizes an aluminum oxide (Al_2O_3) ceramic tube with a tin dioxide (SnO_2) sensitivity layer that changes conductivity in the presence of the gas [11,12]. The static input-to-output model of a MOX sensor that relates the explosive lower limit (LEL) value E in percent (%) to the sensor output voltage V_s is

$$E_{\text{MOX}} = c_1 e^{c_2 V_s} \tag{1}$$

where c_1 and c_2 are experimentally determined constants.

The NDIR gas sensor operates on the notion that many gases exhibit significant absorption of light within the infrared spectrum [13]. Using narrow-band transmission filters, a specific wavelength band of infrared associated with the detection of a specific gas can be isolated. The gas concentration C measured by an NDIR sensor is given by [14]

$$C = \frac{c_0 V_b}{V_{a0} V_{b0}} \Delta V_a \tag{2}$$

where ΔV_a is the sensor output voltage drop, V_{a0} is the voltage drop during calibration measurements upon exposure to a test gas of known concentration c_0, and V_b and V_{b0} are voltage signals from a reference sensor during calibration. The explosive lower limit E is then given by

$$E_{\text{NDIR}} = c_3(V_s - c_4) \tag{3}$$

where c_3 and c_4 are experimentally determined constants.

The MPS is a flammable gas sensor and it consists of an array of MEMS-fabricated microhotplates, each coated with semi-selective polymers. The microplates are heated and their thermal properties are used to determine the concentration and identity of the analyte. The MPS has the ability to detect and classify a wide range of flammable gases, including: methane, propane, butane, ethane, ethylene, hexane, hydrogen, isopropanol, pentane, propylene, toluene, and xylene, at concentrations from 1% to 100% of their respective LEL values. The MPS is a low power device and it does not require calibration; and it also reports atmospheric pressure, temperature, and humidity.

A chemical gas sensor when exposed to a constant gas concentration C_0 initially responds, typically exhibiting low-order dynamics [5]. In the absence of a gas, a sensor's recovery dynamics can also be modeled by a low-order dynamics model. The rise and recovery dynamics can often differ depending on the type of sensor. Motivated by this observation, the dynamics of a gas sensor can be modeled by the following Lapace transform equation (see Fig. 3):

$$G_i(s) = \frac{Y(s)}{C(s)} = \frac{\alpha_i}{\tau_i s + 1}, \quad \tau_i = \begin{cases} \tau_{\text{rise}}, & \dot{c}(t) > 0 \\ \tau_{\text{rec}}, & \dot{c}(t) \le 0 \end{cases} \tag{4}$$

where i denotes rise or recovery phase, $Y(s)$ represents the expected sensor output for a given input chemical gas concentration $C(s)$, and α_i and τ_i are the constants associated with the rise or recovery dynamics. The rise and recovery time constants τ_{rise} and τ_{rec},

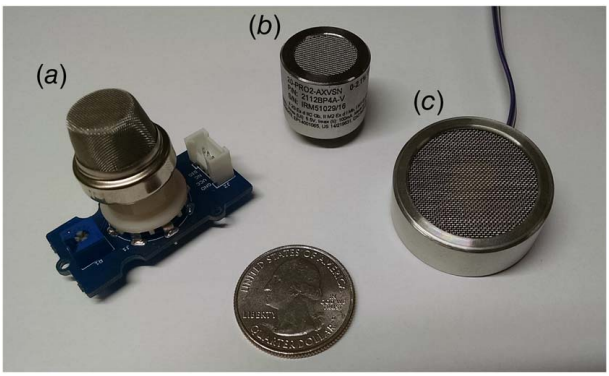

Fig. 2 Gas sensors: (*a*) MOX, (*b*) NDIR, and (*c*) MPS

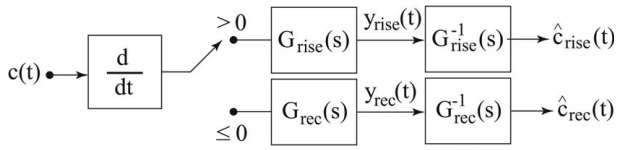

Fig. 3 Sensor model and inverse compensation

respectively, can be determined by the 90% rise time, $T_{90,i}$, from sensor characterization,

$$\tau_i = \frac{T_{90,i}}{-\ln(0.1)} \approx \frac{T_{90,i}}{2.3026} \tag{5}$$

2.2 Maximum Mobile-Sensor Mapping Speed. Creating chemical concentration maps that represent the spatial distribution of a gas plume requires the sensor to be rastered over a desired area. Figure 4 shows an example of this process involving a UAV carrying a gas sensor. The spatial and temporal resolution of the placement of the sensor determines the overall quality of the chemical concentration map. Sensor and vehicle dynamics can lead to distortions in the chemical maps. To determine the maximum mapping speed, it is first assumed that the dynamics of the mobile platform carrying the gas sensor is sufficiently fast compared to the dynamics of the sensor.

Given the dynamics of the sensor in Eq. (4), the practical maximum operating frequency ω_c is related to the rise and recovery time constant τ_i by

$$\omega_c = \beta \frac{1}{\tau_i} \tag{6}$$

where $\beta = 0.1$ (operating at 1/10 of ω_c). For a maximum travel distance of $x_{\max}$, the upper limit on travel speed is

$$v_{\max} = \frac{\beta x_{\max}}{2\pi\tau_i} = \frac{x_{\max}}{20\pi\tau_i} \tag{7}$$

Raster-scanning above the speed $v_{\max}$ leads to distorted chemical maps caused by gas-sensor dynamics. The dynamics-related distortions also appear in other applications such as scanning probe microscopy [15].

2.3 Improving Speed by Sensor Dynamics Compensation. To account for the sensor dynamics and improve mapping speed, feedforward compensation is used (see Fig. 3). For a given rise or recovery sensor time constant τ_i, the feedforward compensator takes the form

$$G_i^{-1}(s) = k\frac{\sigma(\tau_i s + 1)}{\alpha_i(\gamma s + 1)} \tag{8}$$

where σ and γ are appropriately chosen constants based on the rise or recovery dynamics of the sensor, and k is a calibration constant. Essentially, the constants are chosen to account for the DC gain of the gas sensor model given in Eq. (4). The compensator (8) is found by cascading an inverse of the gas-sensor dynamics model given by Eq. (4) with a low-pass filter with time constant $1/\gamma$. This form creates an inverse model that compensates for the gas-sensor dynamics. It is pointed out that for practical implementation, the sensor time constant can be chosen as an average, τ_{ave}, between the rise and recovery dynamics.

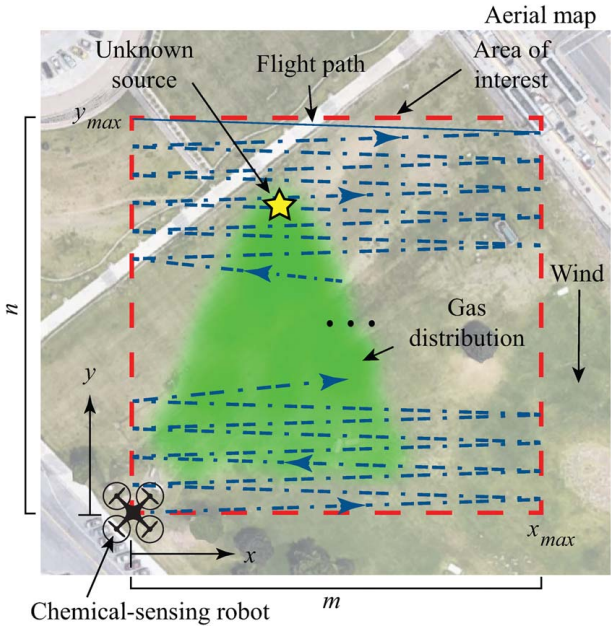

Fig. 4 Raster-scan flight path for chemical mapping, where *m* and *n* refer to the number of sample points along the *x* and *y* directions, respectively

2.4 Particle Swarm Optimization for Source Localization. Particle swarm optimization (PSO) [16] with feedforward compensation is used to localize a plume source. Let $\mathbf{x}_i[k] = [x_i[k], y_i[k]]$ denote the two-dimensional position of the ith mobile sensor at time-step k. The position update law is chosen as

$$\mathbf{x}_i[k+1] = \mathbf{x}_i[k] + \mathbf{v}_i[k+1]\Delta \tag{9}$$

where Δ is the time interval between updates and the velocity term $\mathbf{v_i}[k+1]$ is given by

$$\mathbf{v}_i[k+1] = \Gamma_i[k]\mathbf{v}_i[k] + a_1\left(\frac{\mathbf{p}_i[k] - \mathbf{x}_i[k]}{\Delta}\right)r_1 + a_2\left(\frac{\mathbf{g}[k] - \mathbf{x}_i[k]}{\Delta}\right)r_2 \tag{10}$$

In Eq. (10), $\mathbf{p}_i[k]$ denotes the location of the ith agent's (particle's) "personal best" or highest measured gas concentration, $\mathbf{g}[k]$ is the location of the highest measured gas concentration across all agents (global best), and constants r_1, $r_2 \in \mathcal{U}(0, 1)$ are sampled from a uniform distribution. The cognitive and social coefficients are chosen as $a_1 = 2$ and $a_2 = 2$, respectively, based on prior work [17–19]. The velocity update term $\mathbf{v}_i[k+1]$ consists of three distinct components. The first incorporates the agent's current velocity to drive the agent along its current direction (inertia term), weighted by the stochastic term $\Gamma[k] = 0.5d_1 + 0.5h$, where $h = 4d_1(1 - d_2)$ and constants d_1, $d_2 \in \mathcal{U}(0, 1)$ are sampled from a uniform distribution. Such a term is used to improve convergence compared to using a constant weight [16]. The second component incorporates the agent's personal performance, weighted by constant a_1 and stochastic factor r_1. Finally, the third component captures the collective interaction across all agents (global best), weighted by constant a_2 and stochastic factor r_2. The performance of the PSO algorithm will be studied in conjunction with the sensor dynamics compensation term given by Eq. (8).

2.5 Gas-Plume Dispersion Models. Two distinct gas-plume dispersion models are used to represent the source behavior. The first is the time-invariant or time-averaged Gaussian plume model, given by

$$C(x, y, z) = \frac{Q}{u}\left[\frac{e^{-y^2/2\sigma_y^2}}{\sigma_y\sqrt{2\pi}}\right]\left[\frac{e^{-(z-H)^2/2\sigma_z^2} + e^{-(z+H)^2/2\sigma_z^2}}{\sigma_z\sqrt{2\pi}}\right] \tag{11}$$

where C is gas concentration at a location x downwind from the source location, y horizontal offset from the plume centerline, and z height above the ground surface in the plume frame [6]. Additionally, $Q = 6$ g/s represents the gas release rate, $u = 1.5$ m/s represents the wind speed, oriented along the plume centerline, and $H = 5$ m denotes the height of the emission centerline above the ground surface. The terms σ_y and σ_z are the standard deviations associated with the plume distribution in the horizontal and vertical directions, respectively, given by

$$\sigma_y(x) = e^{(I_y + J_y \ln x + K_y[\ln x]^2)}], \tag{12}$$

$$\sigma_z(x) = e^{(I_z + J_z \ln x + K_z [\ln x]^2)} \quad (13)$$

where $I_y = -3.143$, $J_y = 1.0148$, $K_y = -0.007$, $I_z = -4.49$, $J_z = 1.4024$, and $K_z = -0.054$ are coefficients associated with the atmospheric stability class for the environment modeled [20].

Second, the Quick Urban and Industrial Complex (QUIC) dispersion model is used to produce a more realistic time-dependent plume over flat terrain by modeling the stochastic nature of real plumes [21]. The model computes the three-dimensional (3D) turbulent atmospheric boundary-layer wind fields using a mass-consistent wind model. A simplified form of the Langevin equations is solved to compute the advection and diffusion of passive scalars in a Lagrangian reference frame. The parameters chosen in the model include: release rate $Q = 6$ g/s, wind speed $u = 1.5$ m/s, 122,400 total number of particles, time-step of 0.1 s, concentration average time of 0.5 s, volume of 12 m by 10 m by 10 m, and map resolution in x, y, and z as 0.125, 0.125, and 0.1, respectively.

The environment considered here is obstacle free, providing an environment consistent with that used in the Gaussian plume case. The 3D data set from the QUIC model is used to extract the two-dimensional plume behavior.

3 Simulation and Experimental Results

3.1 Sensor Characterization and Modeling. The three gas sensors are characterized by experimentally measuring rise and recovery response, followed by identifying the model parameters. The experimental setup is shown in Fig. 5, where the gas delivery system has two separate chambers. The first chamber establishes a baseline environment—zeroing-out the sensor—using the synthetic air product Zero Air (ZA). The second chamber creates a desired LEL environment, where ZA product is mixed with undiluted test gas, such as propane, through an Environics 4040 gas dilution system with a flowrate of 300 mL/ min. This process creates gas concentrations of 5%, 10%, 25%, and 50% LEL. The ZA product is supplied to each sensor prior to and after application of the test gas with flow regulated at 400 mL/ min. Measurements are taken as the propane test gas continuously fills the second chamber. Prior to the tests, the MOX sensor is preheated for over 24 h, in accordance with the recommendation provided in the sensor's technical data sheet. Five trials are conducted at each concentration level and the results are averaged. Figure 6 shows the responses, for example, from the three sensors subjected to 50% LEL gas. The responses for all tests showed similar time-response behavior. In particular, the initial exposure to test gas yields a first-order-like output response. Likewise, when the gas is removed the response decays in a similar first-order fashion.

A summary of the measured sensor characteristics are shown in Fig. 7, which include the T_{90}-rise times, T_{90}-recovery times, rise time constants, and recovery time constants. It is noted that the MOX and NDIR sensors exhibit significant differences in characteristics as the gas concentration changes, whereas the MPS remains relatively consistent. From the results obtained, the average calibration factor k for the MOX, NDIR, and MPS are cacu-lated as 0.9228, 1.1242, and 0.9561, respectively.

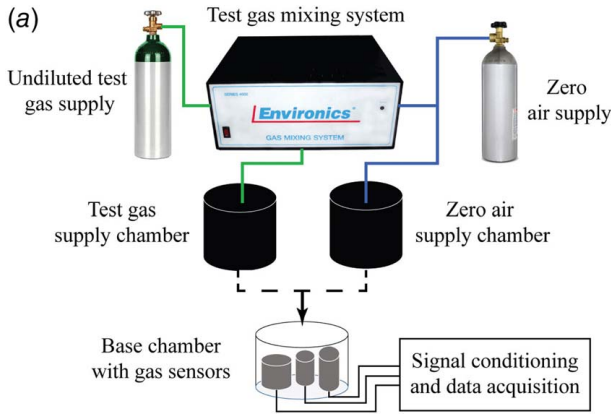

Fig. 5 Experimental setup for sensor characterization

3.2 Gas Distribution Mapping Results. Gas distribution mapping simulations are performed to study the effects of gas-sensor dynamics compensation, based on the characterization results. Simulation studies are considered because a consistent gas source can be created for systematically evaluating the effects of gas-sensor dynamics on mapping. All simulations are created in MATLAB, where the Gaussian and QUIC gas-plume models are used to simulate the gas sources. The mapping process follows a predefined crosswind raster-scan trajectory that covers the desired

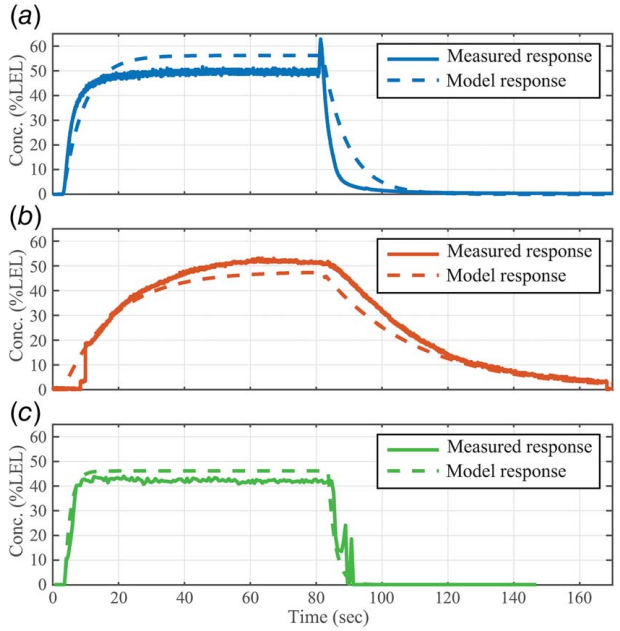

Fig. 6 Examples of experimentally-measured rise and fall time responses compared to model response for (*a*) MOX, (*b*) NDIR, and (*c*) MPS sensor exposed to 50% LEL propane gas

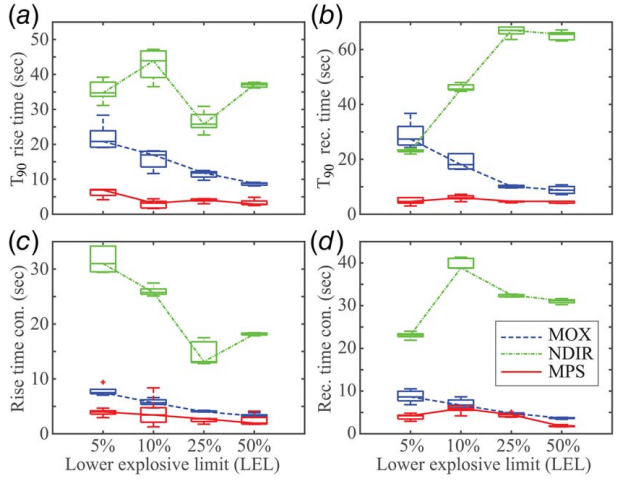

Fig. 7 Comparison of sensor characteristics: (*a*) T_{90}-rise response times, (*b*) T_{90}-recovery times, (*c*) rise time constants, and (*d*) recovery time constants

area of interest (see Fig. 4), consistent with state-of-the-art approaches [22]. Such a trajectory increases the likelihood of finding the location of an unknown leaking-gas source [23].

First, to illustrate the sensor dynamic effects on mapping distortion, Figs. 8(*a*1)–8(*c*1) summarizes the results for raster-scanning at low-speed (0.01 m/s), where Figs. 8(*a*1), 8(*b*1), and 8(*c*1) are associated with the MOX, NDIR, and MPS sensor, respectively. Likewise, the results at high-speed (0.5 m/s, speed exceeding the limit established by Eq. (7)) for the MOX, NDIR, and MPS sensors are shown in Figs. 8(*a*2), 8(*b*2), and 8(*c*2), respectively. It is noted that the upper limit on the travel speed (v_{max}) for each sensor is determined by the rise or recovery time constant as illustrated in Eq. (7). For example, for a scan range of 5 m, the v_{max} values for NDIR, MOX, and MPS sensor are 0.0028 m/s, 0.011 m/s, and 0.037 m/s, respectively. Because the NDIR sensor has the slowest response time, even scanning at 0.01 m/s, there is significant distortion in the gas distribution map as shown in Fig. 8(*b*1). At higher speeds, all three sensors if used for gas distribution mapping show significant distortion as illustrated in Figs. 8(*a*2)–8(*c*2), evident by the smeared concentration distributions.

Using feedforward dynamics compensation through Eq. (8), the mapping distortion due to sensor dynamics at high-speed can be significantly reduced. For example, the results in Figs. 9(*a*1)–9(*c*1) show mapping at low ($0.1v_{max}$), medium (v_{max}), and high ($5v_{max}$) speed, respectively, for the MPS sensor without compensation. As the scan-speed increases, distortion becomes noticeable as shown in Figs. 9(*b*1) and 9(*c*1). The distortion is minimized with feedforward compensation as illustrated in Fig. 9(*a*2) (v_{max}) through 9(*c*2) ($5v_{max}$), where the ground-truth distribution shown in Fig. 9(*a*1) is essentially recovered. As further summarized in Fig. 10 for the MPS sensor, feedforward compensation of gas-sensor dynamics show significant reduction of the RMS mapping error, defined as

$$e_{RMS}(\%) = \frac{\sqrt{\sum_{j=1}^{n}\sum_{i=1}^{m}(C(x_i, y_j) - \hat{C}(x_i, y_j))^2}}{\max(C)} \times 100 \tag{14}$$

In Eq. (14), C denotes the ground-truth chemical distribution given by the Gaussian plume model and $\hat{C}$ is the distribution

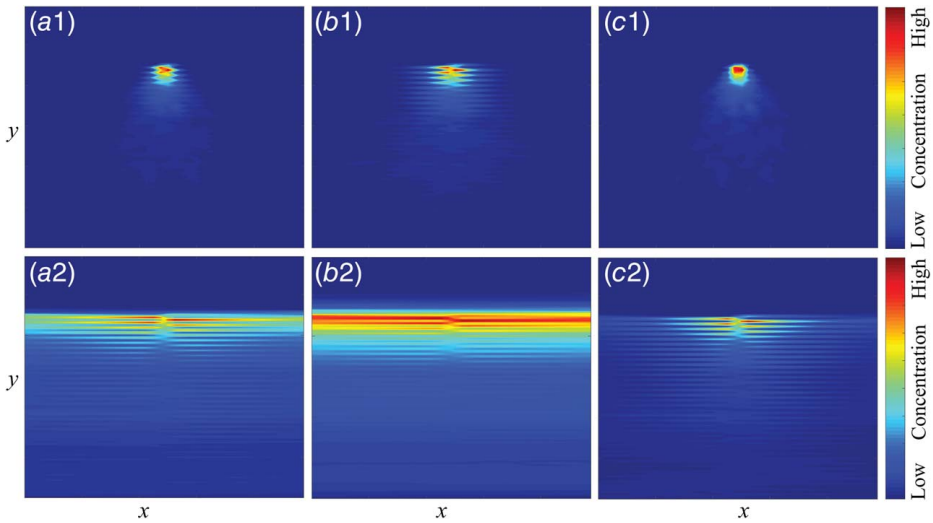

Fig. 8 Mapping results for QUIC plume source at (*a*1−*c*1) low-speed (0.01 m/s) and (*a*2−*c*2) high-speed (0.5 *m*/*s*). (*a*) MOX, (*b*) NDIR, and (*c*) MPS sensor

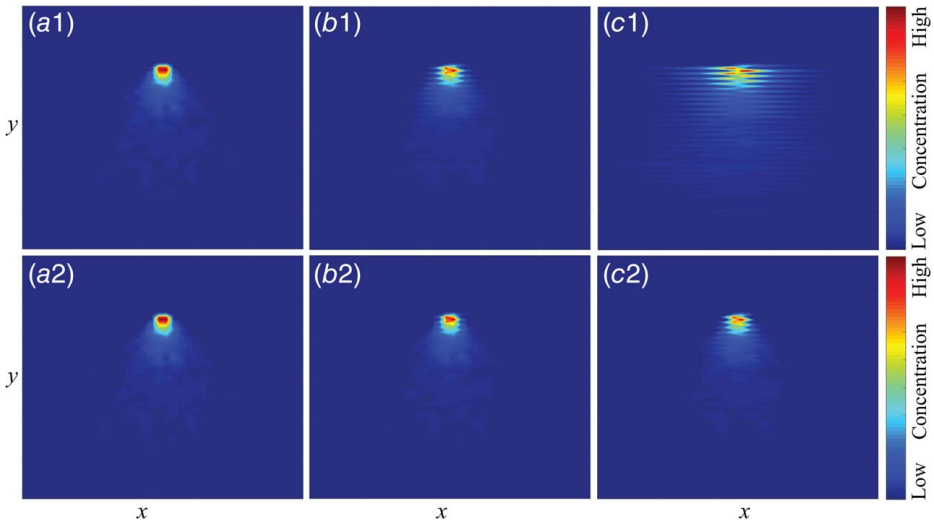

Fig. 9 Mapping results for QUIC plume source: (*a*1 − *c*1) without and (*a*2 − *c*2) with MPS-dynamics compensation

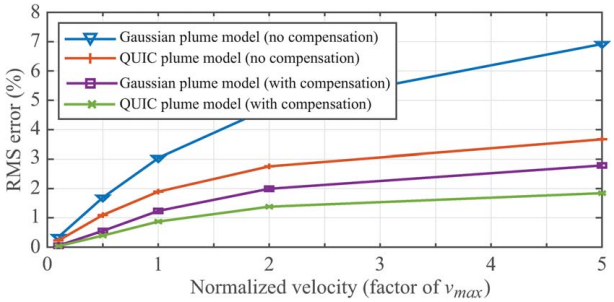

Fig. 10 RMS error comparison for MPS sensor

obtained using the MPS with gas-sensor dynamics compensation. The constants m and n denote the number of sample points along the x and y directions, respectively. These results underscore the importance of feedforward compensation to improve mapping speed.

3.3 Source Localization Via Particle Swarm Optimization Results. The performance of PSO to localize the gas source [24], without and with gas-sensor dynamics compensation, is evaluated based on the following metrics: (1) success rate (SR), the percentage of test runs in which the final position associated with the global best (highest measured concentration), g, falls within 1 m of the position of the actual highest gas concentration; (2) success–failure rate (SFR), the number of tests in which g fell within 1 m of the position of the true highest concentration at any point during the experiment and no longer within this radius when the test is terminated. This metric provides an intuitive sense for the accuracy and stability of g; (3) average failed distance (AFD), represents the average Euclidean distance between the position associated with g and the location of the true highest concentration associated with failed test cases; and (4) average time (AT) required for g to arrive within 1 m of the true highest concentration position.

Table 1 Particle swarm optimization results

Uncompensated with Gaussian plume source					Uncompensated with QUIC plume source				
	SR (%)	SFR (%)	AFD (m)	AT (s)		SR (%)	SFR (%)	AFD (m)	AT (s)
MOX	9	54	5.3	574.6	MOX	11	30	24.0	88.1
NDIR	4	33	19.6	169.5	NDIR	4	24	25.0	61.9
MPS	58	42	1.2	215.6	MPS	43	24	22.2	205.2
Compensated with Gaussian plume source					Compensated with QUIC plume source				
	SR (%)	SFR (%)	AFD (m)	AT (s)		SR (%)	SFR (%)	AFD (m)	AT (s)
MOX	100	0	0.0	121.4	MOX	55	14	27.3	120.7
NDIR	64	36	1.2	199.6	NDIR	53	14	26.1	128.7
MPS	100	0	0.0	104.5	MPS	68	1	35.8	88.8

The simulation-based results for PSO using the MPS, MOX, and NDIR sensors are summarized in Table 1, where the Gaussian and dynamic QUIC plume models are used to model the source. For each source, 100 simulation trials were performed with three agents placed at randomized start locations. The simulated time interval for each run was scaled to represent a realistic flight time for an aerial-based vehicle carrying a gas sensor. The time interval chosen is 40 minutes. The chosen representative result for the NDIR sensor is shown in Fig. 11, where Fig. 11(*a*) shows the environment with plume source and the starting locations of agents relative to plume source, and the PSO performance without and with sensor dynamics compensation are shown in Figs. 11(*b*) and 11(*c*), respectively. It is shown that gas-sensor dynamics compensation enables the mobile sensors to more accurately estimate and localize the source.

The results clearly show improvements of incorporating gas-sensor dynamics compensation. For example, the success rates across all three sensors improved with gas-sensor dynamics compensation compared to the uncompensated case, with an average improvement of approximately 64% and 39% for the Gaussian and QUIC model, respectively. The PSO's performance in terms of converging to the location of the actual highest gas concentration and remaining within a 1-m distance of the source location improved significantly, indicated by the reduction of the SFR value. For the Gaussian plume-source model, the average failed distance and average time to be within 1 m of the source also reduced significantly. However, the AT value for the slower NDIR sensor did not see a reduction in this value.

When the plume source exhibits dynamic effects as modeled by the dynamic QUIC source, it is observed that the AFD and AT values may not improve with gas-sensor dynamics compensation to the same extent as found for the Gaussian plume scenario. This may be caused by the PSO algorithm's retention of the global and personal best values, irrespective of time. For a more dynamic

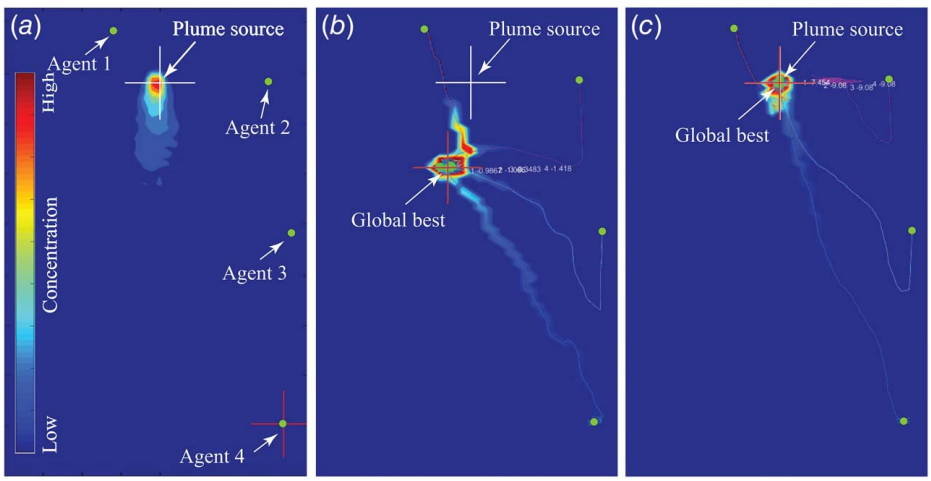

Fig. 11 PSO performance with NDIR sensor: (*a*) environment with gas source and starting locations of agents relative to source, and PSO performance (*b*) without and, (*c*) with sensor dynamics compensation

source, gas concentration value measured at some instant in time may not be indicative of the mean concentration of the plume at a given location. Thus, the measurement may be incorrectly associated with the global best and thereby may misinform the actions taken. To avoid this issue, one possible solution is to average the measurements; however, filtering methods can introduce additional delay and ultimately affect the PSO process.

4 Conclusions

By characterizing, modeling, and compensating for gas-sensor dynamics, the speed, accuracy, and robustness of aerial-based chemical plume mapping and source localization can be significantly improved. Results demonstrate the ability of the method to enable chemical-sensing robots to travel faster during the GDM process while preserving the spatial accuracy of resulting maps. Furthermore, feedforward compensation of sensor dynamics significantly improves, by as much as 64%, the success rate of particle swarm optimization for gas source localization.

Acknowledgment

The authors acknowledge support from the Dept. of Defense SMART Scholarship Program, the National Science Foundations Partnership for Innovation Program (Grant No. 1430328), and U.S. ARMY STTR Program Grant No. W9132T-16-C-0001.

Conflict of Interest

There are no conflicts of interest.

Data Availability Statement

The datasets generated and supporting the findings of this article are obtainable from the corresponding author upon reasonable request.

References

[1] Hutchinson, M., Oh, H., and Chen, W.-H., 2017, "A Review of Source Term Estimation Methods for Atmospheric Dispersion Events Using Static Or Mobile Sensors," Inf. Fusion, **36**(36), pp. 130–148.

[2] Neumann, P. P., Bennetts, V. H., Lilienthal, A. J., Bartholmai, M., and Schiller, J. H., 2013, "Gas Source Localization With a Micro-Drone Using Bio-Inspired and Particle Filter-Based Algorithms," Adv. Rob., **27**(9), pp. 725–738.

[3] Kowadlo, G., and Russell, R. A., 2008, "Robot Odor Localization: A Taxonomy and Survey," Int. J. Rob. Res., **27**(8), pp. 869–894.

[4] Rossi, M., and Brunelli, D., 2016, "Autonomous Gas Detection and Mapping With Unmanned Aerial Vehicles," IEEE Trans. Inst. Meas., **65**(4), pp. 765–775.

[5] He, X., Bourne, J. R., Steiner, J. A., Mortensen, C., Hoffman, K. C., Dudley, C. J., Rogers, B., Cropek, D. M., and Leang, K. K., 2019, "Autonomous Chemical Sensing Aerial Robot for Urban/Suburban Environmental Monitoring," IEEE Syst. J., **13**(3), pp. 3524–3535.

[6] Bourne, J. R., Goodell, M., He, X., Steiner, J., and Leang, K. K., 2020, "Decentralized Multi-Agent Information-Theoretic Control for Target Estimation and Localization: Finding Chemical Leaks," Int. J. Rob. Res., **39**(13), pp. 1525–1548.

[7] Fu, H.-L., Chen, H.-C., and Lin, P., 2012, "APS: Distributed Air Pollution Sensing System on Wireless Sensor and Robot Networks," Comput. Commun., **35**(9), pp. 1141–1150.

[8] Lilienthal, A. J., Loutfi, A., and Duckett, T., 2006, "Airborne Chemical Sensing With Mobile Robots," Sensors, **6**(11), pp. 1616–1678.

[9] Gatti, M., Giulietti, F., and Turci, M., 2015, "Maximum Endurance for Battery-Powered Rotary-Wing Aircraft," Aerosp. Sci. Technol., **45**, pp. 174–179.

[10] Meng, Q.-H., Yang, W.-X., Wang, Y., and Zeng, M., 2011, "Collective Odor Source Estimation and Search in Time-Variant Airflow Environments Using Mobile Robots," Sensors, **11**(11), pp. 10415–10443.

[11] Arshak, K., Moore, E., Lyons, G., Harris, J., and Clifford, S., 2004, "A Review of Gas Sensors Employed in Electronic Nose Applications," Sensor Rev., **24**(2), pp. 181–198.

[12] Monroy, J. G., Gonzalez-Jimenez, J., and Blanco, J. L., 2012, "Overcoming the Slow Recovery of MOX Gas Sensors Through a System Modeling Approach," Sensors, **12**(10), pp. 13664–13680.

[13] Gibson, D., and MacGregor, C., 2013, "A Novel Solid State Non-Dispersive Infrared CO2 Gas Sensor Compatible With Wireless and Portable Deploy," Sensors, **13**(6), pp. 7079–7103.

[14] Sun, H. T., and Hsi, P. C., 2002, "Non-Dispersive Infrared Gas Sensor." US Patent 6,469,303.

[15] Yong, Y., Moheimani, S. O. R., Kenton, B. J., and Leang, K. K., 2012, "Invited Review: High-Speed Flexure-Guided Nanopositioning: Mechanical Design and Control Issues," Rev. Sci. Instrum., **83**(12), p. 121101.

[16] Feng, Y., Teng, G.-F., Wang, A.-X., and Yao, Y.-M., 2007, "Chaotic Inertia Weight in Particle Swarm Optimization," Second IEEE International Conference on Innovative Computing, Kumamoto, Japan, Sept. 5–7, p. 475–475.

[17] Marini, F., and Walczak, B., 2015, "Particle Swarm Optimization (PSO). A Tutorial," Chemometr. Intell. Lab. Syst., **149**, pp. 153–165.

[18] Ozcan, E., and Mohan, C. K., 1998, "Analysis of a Simple Particle Swarm Optimization System," Intell. Eng. Syst. Through Artif. Neural Netw., **8**, pp. 253–258.

[19] Kennedy, J., and Eberhart, R., 1995, "Particle Swarm Optimization," Proceedings of the IEEE International Conference on Neural Networks, Perth, WA, Australia, Nov. 27–Dec. 1, Vol. 4, pp. 1942–1948.

[20] Hanna, S. R., Briggs, G. A., and Hosker Jr, R. P., 1982, *H*andbook on Atmospheric Diffusion. National Oceanic and Atmospheric Administration, Oak Ridge, TN, USA. Atm. Turbulence and Diff. Lab.

[21] Singh, B., Pardyjak, E. R., Norgren, A., and Willemsen, P., 2011, "Accelerating Urban Fast Response Lagrangian Dispersion Simulations Using Inexpensive Graphics Processor Parallelism," Env. Model. Soft., **26**(6), pp. 739–750.

[22] Pasternak, Z., Bartumeus, F., and Grasso, F. W., 2009, "Lévy-Taxis: A Novel Search Strategy for Finding Odor Plumes in Turbulent Flow-Dominated Environments," J. Phys. A: Math. Theor., **42**(43), p. 434010.

[23] Marjovi, A., and Marques, L., 2014, "Optimal Swarm Formation for Odor Plume Finding," IEEE Trans. Cybern., **44**(12), pp. 2302–2315.

[24] Gunawardena, N., Leang, K. K., and Pardyjak, E., 2021, "Particle Swarm Optimization for Source Localization in Realistic Complex Urban Environments," Atmos. Environ., **262**, p. 118636.